Solar Energy Materials & Solar Cells 260 (2023) 112478

Contents lists available at ScienceDirect

Solar Energy Materials and Solar Cells

journal homepage: www.elsevier.com/locate/solmat

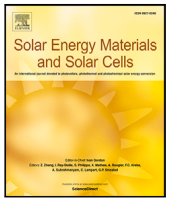

Efficiency enhancement of solar cell by using methylammonium lead tribromide/polymethyl methacrylate hybrid film as luminescent down shifting layer

Jiayao Xu [a], Wei Pan [a,*], Wenzhong Shen [a,b,*]

[a] Institute of Solar Energy, and Key Laboratory of Artificial Structures and Quantum Control (Ministry of Education), School of Physics and Astronomy, Shanghai Jiao Tong University, Shanghai 200240, People's Republic of China

[b] Shanghai Non-carbon Energy Conversion and Utilization Institute, Shanghai 200240, People's Republic of China

ARTICLE INFO

Keywords:
$MAPbBr_3$
Efficiency enhancement
Luminescent down-shifting
Antireflection
Si solar cell

ABSTRACT

Luminescent down-shifting (LDS) layer was introduced to tackle the issue of poor short-wavelength response of solar cell. Besides LDS effect, coating a LDS layer on the surface of a solar cell leads to a change in surface reflectance. LDS and antireflection (AR) effect are coupled and usually reported as a single effect. For those solar cell with optimized AR, it is difficult to enhance power conversion efficiency (PCE) with the LDS layer due to the variation of reflectance. In this work, we report an obvious PCE enhancement of two mainstream commercial silicon (Si) solar cells with the optimized AR by using methylammonium lead tribromide ($MAPbBr_3$)/polymethyl methacrylate (PMMA) hybrid film as a LDS layer. The used $MAPbBr_3$/PMMA nanoplatelets solutions for LDS layer have an absolute photoluminescent quantum yield of ~85 % (excited by 350 nm) in air atmosphere for more than 30 days, laying a foundation for the realization of effective LDS effect. Theoretical analysis has separated the AR and LDS effect. It has demonstrated that AR effect has a positive influence on LDS effect, and PMMA plays the key role in the improvement of AR. Experimental studies further elucidated the LDS and AR effect provided by $MAPbBr_3$/PMMA hybrid film. Thanks to this combined effect, the application of $MAPbBr_3$/PMMA hybrid film as a LDS layer on Si heterojunction solar cell yields a PCE gain of 0.3 % absolute and that on passivated emitter and rear cell produces an absolute PCE enhancement of about 0.7 %.

1. Introduction

Solar energy is one of the most potential environment-friendly energies, whose radiation level on the earth's surface is as high as 1.8×10^{14} kW [1,2]. Solar cells can directly convert solar energy into electricity, offering a clean and sustainable solution to meet ever-increasing global energy demands. However, poor spectral response in the UV-blue region of solar cell becomes a barrier for achieving a higher power conversion efficiency (PCE) of commercial solar cells [3–5]. In 1979, luminescent down-shifting (LDS) of the incident solar spectrum was introduced to tackle this issue by converting short-λ photons into long-ones for more efficient utilization of the entire solar spectrum [6]. After that, many research have demonstrated that the coating of LDS layer on various solar cells significantly enhanced short-circuit current density (J_{sc}), external quantum efficiency (EQE) in whole wavelength range, and thus PCE [7–14]. Nonetheless, these LDS coated solar cell did not exhibit high PCE due to their lower initial PCE. Seldom work reported the effective LDS effect on the high-performance mainstream silicon (Si) photovoltaic (PV) cell, such as Si hetero-junction (SHJ) solar cell and passivated emitter and rear cell (PERC), although theoretical analysis [15] have pointed out that the calculated PCE enhancement of Si-based solar cell due to an "ideal" LDS process is about 0.6% absolute.

Previous theoretical simulations [16,17] assume that LDS layer does not cause a change in reflectance, but experimental studies [8,18,19] have indicated that the significant enhancement of PCE comes from not only LDS effect, but anti-reflection (AR) effect, since EQE shows an increase in all wavelengths. The surface of mainstream Si based cells are usually textured for optimized AR with different micro-structures, such as pyramid arrays [20], nanowire arrays [21], and nanopores [22]. This surface texturization makes it challenging to improve the AR and PCE by using LDS layer. Further improvements in Si cell performance through LDS technology is possibly achieved by increasing the LDS efficiency [23] and/or by improving the AR effect [24]. For example, recently, Jiang et al. [24] reported an enhancement of 0.28% absolute through thermal evaporating MgF_2 anti-reflection layer on CdSe/ZnS

* Corresponding authors.
E-mail addresses: sjtushelwill@sjtu.edu.cn (W. Pan), wzshen@sjtu.edu.cn (W. Shen).

https://doi.org/10.1016/j.solmat.2023.112478
Received 11 April 2023; Received in revised form 7 June 2023; Accepted 23 July 2023
Available online 2 August 2023

quantum dots (QDs) LDS layer grown on SHJ solar cell by ink-jet printing technology.

Besides the AR, the down-shifting efficiency of LDS layer is another important factor affecting the PCE enhancement. QDs are popular candidates for LDS material because of wide absorption bands and tunable emission bands, large stokes shift, and high photoluminescence (PL) quantum yield (QY) [25]. Among QDs, organometal halide perovskites like $CH_3NH_3PbX_3$ ($MAPbX_3$, X = Br, I, Cl) are interesting owing to the near-unit QY, tunable absorption and emission bands [26], and simple synthetic methods [27,28]. However, perovskites may be degraded when exposed to air, heat, and moisture [29,30]. Many researchers embedded perovskite QDs into bulk materials, like polyvinyl acetate (PVA) [31], polymethyl methacrylate (PMMA) [32,33], polydimethylsiloxane (PDMS) [34,35], Ethylene Vinyl Acetate (EVA) [36], and SiO_2[34], as LDS layers, to prevent the irreversible aggregation of quantum dots and form refractive index gradient to avoid optical loss [37,38]. Their studies have demonstrated obvious improvement of the performance of planar solar cells. Nevertheless, these research did not analyze the coupled contribution of LDS and AR effect of LDS layer on PCE of solar cell, which is crucial to understand the key role of LDS layer and to the optimization of LDS layer on solar cell.

In this work, we report the absolute PCE enhancement of about 0.3% on SHJ solar cell and 0.7% on PERC by using $MAPbBr_3$/PMMA hybrid film as a LDS layer. A facile but effective ligand-assisted reprecipitation (LARP) approach is firstly proposed to synthesize $MAPbBr_3$/PMMA nanoplatelets (NPLs) with a PLQY of over 85% in air atmosphere for more than 30 days. Theoretical simulation then illustrates that AR effect on EQE is greater than that of LDS effect, but both of them are able to be optimized through controlling the thickness of $MAPbBr_3$ and PMMA layer. After that, $MAPbBr_3$/PMMA composite films were integrated with two mainstream commercial Si cells (SHJ cell and PERC) through simple spin coating. Control experiments show a clear distinction between the contributions of LDS and AR. Thanks to the combined effect of LDS and AR, the coating of hybrid film leads to the PCE enhancement of these two kinds of solar cell. This work offers a new perspective of LDS layers coating on solar cells with textured surface.

2. Experimental details

2.1. Materials

Lead bromide ($PbBr_2$, 99.9%) and methylammonium bromide (MABr, 99.%) were purchased from Xi'an Polymer Light Technology Corp. Toluene (anhydrous, 99.5%), Polymethyl methacrylate (PMMA, Molar Weight 15,000), and N,N-Dimethylformamide (DMF, anhydrous, 99.8%) were purchased from Sigma-Aldrich. Phenethylamine (PEA, anhydrous, 99%) was purchased from Acros Organics. Acetic acid (HAc, 98%) and hydrochloric acid (HCl) was purchased from Sinopharm Chemical Reagent Co. Ltd. All the chemicals were used as received without further purification. The commercial PERC and SHJ cells of ~2 cm × 2 cm area were from commercial market and cut by laser cutting technology. The PCE of solar cells after cutting will decrease because of laser scribing and mechanical breaking during laser cutting [39].

2.2. Synthesis of $MAPbBr_3$/PMMA dispersion in toluene and film preparation

The $MAPbBr_3$ NPLs solution were synthesized in nitrogen-filled glovebox by using previously reported LARP method [40] with a little modification on the antisolvent. In a typical synthesis, 0.0476 g of MABr, 0.1835 g of $PbBr_2$, 50 μL of PEA, and 138 μL of HAc were mixed firstly in 5 mL of DMF to form a 0.1 mol/L precursor solution. After that, 20 mg of PMMA was added into 1 mL of toluene with vigorously stirring for more than 24 h to form a 20 mg/mL homogeneous PMMA-toluene antisolvent. 18 μL of precursor solution was then added dropwisely into 1 mL of PMMA-toluene mixed solvent under vigorously stirring for 10 min to obtain a bright greenish $MAPbBr_3$/PMMA-20 dispersion. To explore the effect of PMMA on stability and optical properties of NPLs, the mass of PMMA (x mg) in toluene (1 mL) was controlled from 0 to 40 mg to synthesize the $MAPbBr_3$/PMMA-x dispersion. Finally, cleaned SHJ and PERC solar cell of ~2 cm × 2 cm size were preheated and then the above dispersion was spin-coated onto the surface of PV devices in air atmosphere at a speed of 3500 rounds per minute for 40 s, forming the LDS layer.

2.3. Characterization

The steady state PL spectra, PL decay curves, and absolute PLQY were measured by steady-state Transient Fluorescence Spectrometer with integrating sphere accessory (FLS1000, Edinburgh Instruments UK). The absolute PLQY is then calculated by using the formula of PLQY=I_{em}/I_{abs}, where I_{abs} is the number of photons absorbed and I_{em} is the number of photons emitted. The ultraviolet–visible (UV–Vis) absorption spectra were measured by a Perkin-Elmer (USA) Lambda 20 spectrometer. TEM images were collected by Material Mode Field Emission Transmission Electron Microscopy (Talos F200X G2, Thermo) with accelerating voltage of 200 kV. AFM images were obtained using Atomic Force Microscope (MFP-3D, Oxford Instruments). SEM images were taken with scanning electron microscope (RISE-MAGNA,TESCAN). The current density–voltage (J–V) curves were obtained under AM 1.5G illumination using Keithley 2400 Sourcemeter and solar simulator (Oriel Sol-2A, Newport). The EQE and reflectance spectra of the solar cell were obtained by quantum efficiency measurements (QEX10, PV measurements, USA). The refractive index was measured by Semilab SE-2000 Spectroscopic Ellipsometer.

3. Theoretical model

Theoretical optical model about the effect of LDS layer on the EQE spectra of PV cells had been proposed by Rothemund [17], but he did not consider the variation of reflectance spectra induced by LDS layer. Here, we introduced the reflectance variation and re-described the EQE spectra as,

$$\mathrm{EQE}(\lambda) = [1 - A(\lambda)]\frac{1 - R_1(\lambda)}{1 - R_0(\lambda)}\mathrm{EQE_b}(\lambda) + A(\lambda)[1 - R_1(\lambda)]\eta_{\mathrm{LDS}}(\lambda)\mathrm{EQE_b}(\lambda_{\mathrm{em}}) \tag{1}$$

where $\mathrm{EQE_b}(\lambda)$ is the EQE spectra of solar cell before LDS layer coated, $\eta_{\mathrm{LDS}}(\lambda)$ is the LDS efficiency, $\mathrm{EQE}_b(\lambda_{\mathrm{em}})$ is the EQE value at the emission wavelength of the PL peak of LDS layer, $A(\lambda)$ represents the absorption proportion of LDS layer in the incoming solar spectrum, and $R_0(\lambda)$ and $R_1(\lambda)$ are the reflectance spectra of the cell before and after covered with LDS layer, respectively.

According to the above equation, the change of EQE spectra due to LDS effect ($\Delta\mathrm{EQE_{LDS}}$) and AR effect ($\Delta\mathrm{EQE_{AR}}$) of LDS layer are respectively given by

$$\Delta\mathrm{EQE_{LDS}}(\lambda) = A(\lambda)[1 - R_1(\lambda)]\eta_{\mathrm{LDS}}(\lambda)\mathrm{EQE_b}(\lambda_{\mathrm{em}}) \tag{2a}$$

$$\Delta\mathrm{EQE_{AR}}(\lambda) = [1 - A(\lambda)]\frac{1 - R_1(\lambda)}{1 - R_0(\lambda)}\mathrm{EQE_b}(\lambda) - \mathrm{EQE_b}(\lambda) \tag{2b}$$

The down-shifting efficiency (η_{LDS}) can be modeled by [41]

$$\eta_{\mathrm{LDS}}(\lambda) = \mathrm{PLQY_{QD}}(\lambda)(1 - \eta_{\mathrm{abs}})(1 - \eta_{\mathrm{out}}) \tag{3}$$

where η_{abs} corresponds to the loss due to re-absorption and η_{out} represents output-coupling loss. η_{out} is calculated according to Snell's law, that is, $\eta_{\mathrm{out}} = \frac{1-\cos[\sin^{-1}(\frac{n_{\mathrm{air}}}{n_{\mathrm{PMMA}}})]}{2}$ with the refractive index of air ($n_{\mathrm{air}} \approx 1$) and that of PMMA tested experimentally.

4. Results and discussion

Fig. 1(a) displays TEM image of a typical as-synthesized NPL ($MAPbBr_3$/PMMA-20 dispersions), which has a rectangular structure with a length of ~100 nm and width of ~80 nm. AFM image in Fig. 1(b) further demonstrates the rectangle shape, whose lateral dimension is ~135 nm × 106 nm (in consistence with the TEM result), and thickness is ~5 nm (inset figure). To evaluate the potential photoelectric application of $MAPbBr_3$/PMMA hybrid film, we analyze the absorption and PL spectra of $MAPbBr_3$/PMMA dispersions in toluene synthesized with different amount of PMMA. UV–Vis absorption spectra in Fig. 1(c) show all the NPLs solutions have similar absorption behavior, an exciton absorption peak at ~515 nm corresponding to the perovskite nanosheet with a larger thickness and a relatively weak peak at 410 nm which is the band gap energy of nanosheet with small layers. PL spectra excited by 350 nm in Fig. 1(d) and corresponding information in Fig. S1 demonstrate that as-synthesized $MAPbBr_3$ NPLs solutions have a green emission (see inset of Fig. 1(d)) centered at 528 nm (full width at half maximum, FWHM=26 nm) with an absolute PLQY of ~100%. With the increase of PMMA in toluene, PL spectra shows a slightly blue shift and broadening, to 524 nm and 29 nm (FWHM) for the sample $MAPbBr_3$/PMMA-40. The blueshift of PL spectra are possibly caused by barrier properties of PMMA matrix during nucleation and growth of perovskite crystals. The increase of FWHM may be attributed to aggregation effects and the irregular size of $MAPbBr_3$/PMMA nanosheets [42,43]. Clearly, the addition of PMMA does not change the band structure of perovskite, but it will weaken the PLQY, from 100% (0 mg), to 96% (10 mg), 94% (20 mg), 86% (30 mg), and 78% (40 mg). Although PLQY of NPLs synthesized in high PMMA concentration (e.g., 40 mg/mL) shows a substantial decline (78%), that in moderate PMMA concentration (e.g., 20 mg/mL) is still kept at a high level of 94%, which is suitable for the application on solar cell as a LDS layer [16]. Fig. 1(e) shows the time evolution of PLQY after exposing $MAPbBr_3$/PMMA-x dispersions in atmospheric condition with a temperature of 10~20 °C and a humidity of 60~80%. As observed, PLQY of $MAPbBr_3$/PMMA-0 decreases significantly with time, from initial 100% to 68% after 30 days, but that of $MAPbBr_3$/PMMA-x (x = 10, 20, 30, and 40) drops obviously more slowly. For example, the initial PLQY of $MAPbBr_3$/PMMA-20 dispersions is ~95%, but it still remains ~85% after 30 days of exposure to air. More amount of PMMA, less decay of PLQY with time, indicating the protective role of PMMA. Fig. S2 shows FTIR spectra of PMMA powder, $MAPbBr_3$/PMMA-0, and $MAPbBr_3$/PMMA-20 dispersions. Clearly, $MAPbBr_3$/PMMA-20 dispersions exhibit the typical absorption at ~3170 cm^{-1} (N-H bond stretching) and ~1477 cm^{-1} (C-H bond bending) [44], similar to $MAPbBr_3$/PMMA-0 dispersions. $MAPbBr_3$/PMMA-20 dispersions also display an absorption at ~1732 cm^{-1}, which represents C=O stretching, indicating that $MAPbBr_3$ is possibly bonded with PMMA through chemical interaction [45]. This protection is effective against water erosion, but is easily destroyed by acid, as shown in Figs. S3~S5. Fig. 1(f) gives the PL decay curves of $MAPbBr_3$ NPLs synthesized with different PMMA concentrations at an excitation wavelength of 365 nm. The measured PL decay curves are fitted with two exponential decay functions of $I(t) = I_0 + A_1\exp(-t/\tau_1) + A_2\exp(-t/\tau_2)$, and average fluorescence lifetimes τ_{avg} are calculated by formula of $\tau_{avg} = (A_1\tau_1^2 + A_2\tau_2^2)/(A_1\tau_1 + A_2\tau_2)$. The fitted τ_{avg} were 15.8, 20.3, 20.6, 22.4, and 23.6 ns when the PMMA concentration was 0, 10, 20, 30, and 40 mg/mL, respectively. With the increasing amount of PMMA during the synthesis, τ_{avg} increases, indicating that the polymer chain of PMMA can effectively passivate surface defects, thereby suppresses non-radiative recombination and leads to the increase of PL lifetime [42].

The dispersion of $MAPbBr_3$/PMMA in toluene (20 mg/mL) exhibits a high PLQY of ~95% at an excitation of 350 nm and good circumstance stability, especially against long-time sunlight exposure, as shown in Fig. S6. Hence it is possible to be used as a LDS layer on commercial Si solar cells [16]. To further explore it, we simulated the variation of EQE spectra of SHJ solar cell after coated by LDS layer according to Eqs. (2a)~(2b). The structure diagrams of simulated SHJ solar cell are shown in the inset of Fig. 2. In the simulation process, it is assumed that the coating of LDS layer did not change the surface morphology and the concentration of NPLs will not cause serious self-absorption, which is possibly to reduce the EQE spectra and PCE. The required PLQY is set as 0.95 for 300~520 nm. The $EQE_b(\lambda)$ and n_{PMMA} spectra were obtained from the experimental data by interpolation method with a step of 1 nm (see Figs. S7~S8). The $R_0(\lambda)$, $R_1(\lambda)$, and $A(\lambda)$ were calculated by software of OPAL 2 developed by PV lighthouse [46] with an experimental observed characteristic angle of pyramid of 54.7°. Fig. 2(a) shows the simulated variation of EQE (ΔEQE) spectra of SHJ solar cell after coated by $MAPbBr_3$ with a thickness ranging from 0 to 5 nm and PMMA film with a thickness of 40 nm. As observed, the increasing thickness of $MAPbBr_3$ results in greater improvement of ΔEQE in the 300~400 nm region and a larger decrease in the 400~700 nm, while the long-wave ΔEQE changes are not sensitive to the amount of $MAPbBr_3$. Simulated results in the middle of Fig. 2(a) also illustrate that $MAPbBr_3$ layer indeed brings the enhancement of EQE in the 300~520 nm region, showing an obvious down-shifting effect. On the other hand, the higher refractive index of $MAPbBr_3$ layer ($n_{MAPbBr3}$ = 2.0 ~ 2.4) [47] is disadvantaged to the AR and leads to the final enhancement of reflectance in 400~550 nm, as shown in the bottom of Fig. 2(a). According to Fig. S9, the variation of short-circuit current density ($\Delta J_{sc} = q\int AM_{1.5G}(\lambda)\Delta EQE(\lambda)d\lambda$) is greatest at the lowest $MAPbBr_3$ thickness of 0.1 nm and then we simulated the ΔEQE spectra of SHJ solar cell caused by LDS layer with a fixed $MAPbBr_3$ thickness of 0.1 nm and different thickness of PMMA layer, as shown in the top of Fig. 2(b). Apparently, with the increase of PMMA thickness, ΔEQE in UV and long wavelength range becomes positively larger, and the ΔEQE_{LDS} curves in the middle of Fig. 2(b) show a typical improvement in the 300~440 nm region, whose ΔJ_{sc} is greatest at the simulated PMMA thickness of 60 nm (Fig. S10). The increasing PMMA thickness also causes a significant improvement in ΔEQE_{AR} (see the bottom in Fig. 2(b)). It should be noted that even without the protection of PMMA, ΔJ_{sc} is still positive when the PLQY of $MAPbBr_3$ is equal to 95%. However, AR effect on EQE by coating $MAPbBr_3$/PMMA is greater than that of LDS effect, since reflectance of the solar cell surface determines the photon flux incident into the solar cell, and also the absorbed photo flux by the LDS layer. The improvement of AR also enhance the LDS effect.

Theoretical simulation indicates that for enhancing the efficiency, less luminescent materials and more PMMA is needed. However, experimental results in Fig. 1 have demonstrated the decrease of PLQY with the increasing PMMA concentrations. Therefore, the trade-off lies between the good AR and the high PLQY. $MAPbBr_3$/PMMA-20 NPLs with low concentration was finally chosen for the experiments to avoid the self-absorption phenomenon and the enhancement of reflectance caused by the high concentration of NPLs. The transmittance spectrum of $MAPbBr_3$/PMMA-20 NPLs film with low concentration on a quartz substrate in Fig. S11 shows that the film phase has a similar absorption behavior to the solution phase and an impressively high transmittance >96% in visible-infrared region.

Fig. 3(a) displays $J-V$ curves of commercial SHJ (~2 cm × 2 cm, with ITO anti-reflective layer) before (black) and after (red) coated with $MAPbBr_3$/PMMA-20 hybrid film as LDS layer, together with the PV parameters of open circuit voltage (V_{oc}), J_{sc}, filling factor (FF), and PCE listed in the inset. Notably, the relatively low FF and PCE of SHJ cell are caused by laser scribing and mechanical breaking during laser cutting [39], but its V_{oc} and J_{sc} are still high. Clearly, the coating of LDS layer results in a final PCE gain of 0.32% absolute, comparable to that reported by Jiang et al. [24]. The increase of PCE is also accompanied by the improvement of J_{sc}, increasing from 40.20 mA/cm^2 (before) to 40.59 mA/cm^2 (after). V_{oc} rises subtly from 0.701 V to 0.703 V, and FF increases from 64.18% to 64.46%. Similar increase of FF has

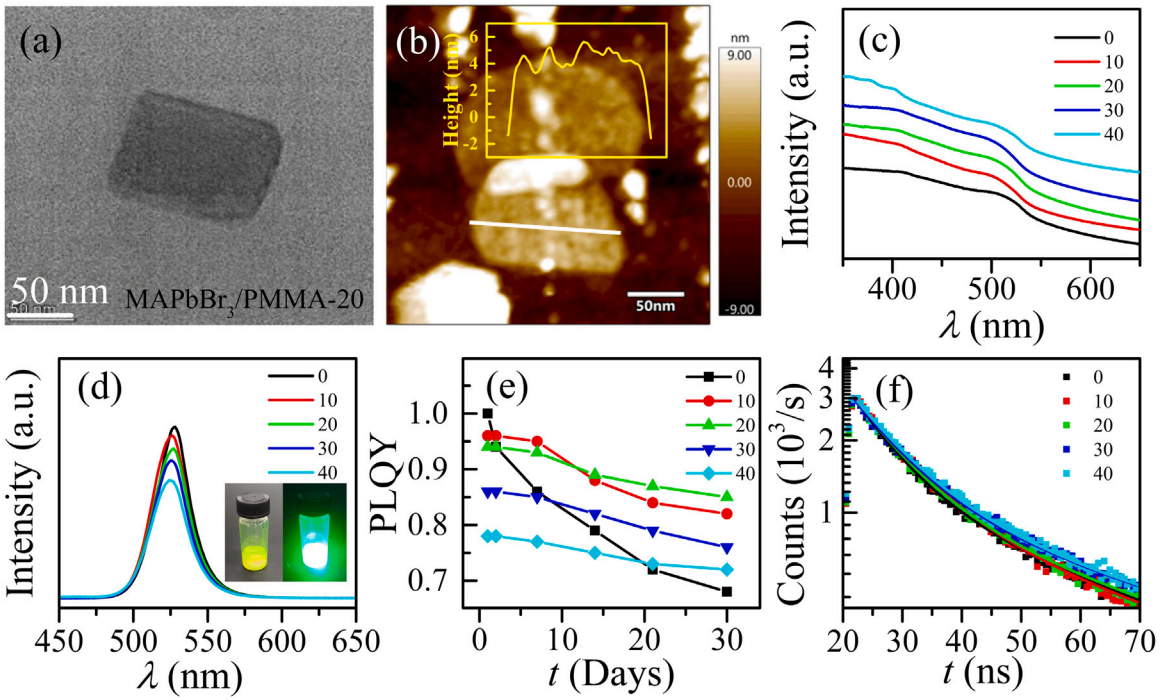

Fig. 1. (a) TEM and (b) AFM image of $MAPbBr_3$/PMMA-20 NPLs. The inset of Fig. 1b is the height profile of a single NPL. (c) Absorption spectra, (d) PL spectra excited by 350 nm, (e) time-evolution of absolute PLQY with an excitation of 350 nm, and (f) PL decay curves monitored at 525 nm with the excitation of 365 nm of $MAPbBr_3$/PMMA-*x* (*x* = 0, 10, 20, 30, and 40) dispersions. The inset of Fig. 1d is the photograph of $MAPbBr_3$/PMMA-20 dispersions under daylight and UV light.

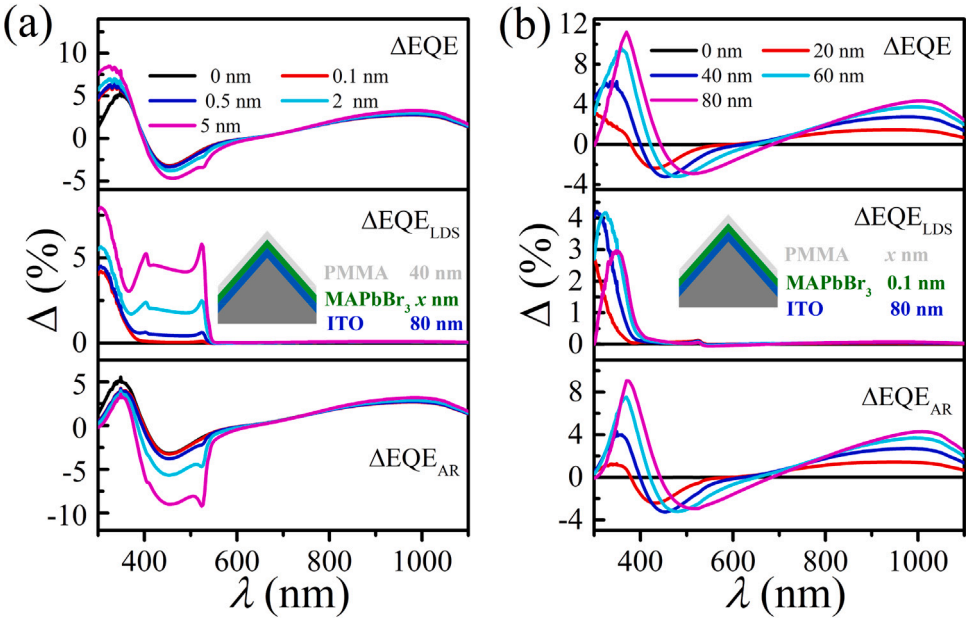

Fig. 2. Simulated ΔEQE (top), ΔEQE_{LDS} (middle), and ΔEQE_{AR} (bottom) of SHJ solar cell after coated by (a) $MAPbBr_3$ with thickness of 0.1~10 nm and PMMA with a thickness of 40 nm; (b) $MAPbBr_3$ with a thickness of 0.1 nm and PMMA with thickness of 10~80 nm.

been reported previously [24]. The slight FF gains possibly thanks to the better lateral conduction of carriers to electrodes [48], since carriers generated by light emitted from LDS layer are mainly located within ~1 μm depth of the silicon surface, contributing to the reduction of the sheet resistance. SEM image in Fig. 3(b) and EDS elemental mapping of lead (Pb, green) in Fig. 3(b′), bromine (Br, red) in Fig. 3(b″) and both of Br and Pb in Fig. S12 show that LDS layer is tightly attached to the textured surface and $MAPbBr_3$ NPLs are uniformly distributed in PMMA, but the characteristic angle of the pyramid shows a slightly decrease. Considering that the surface morphology of LDS film spun on the SHJ cell is mainly decided by the diffusion process of the PMMA/toluene solvent, the decrease of the characteristic angle is possibly from the contribution of PMMA. The cross-sectional SEM image of SHJ cell covered by pure PMMA shown in Fig. S13 also displays the obvious decrease in the characteristic angle. To further explore the effect of uniformly covered LDS layer on the characteristic parameters, we show in Fig. 3(c) the EQE and reflectance (*R*) spectra of SHJ before (black) and after (red) coated with LDS layer. As observed, the application of LDS layer on SHJ solar cell produces an improvement of AR but weak enhancement of EQE only in the wavelength region

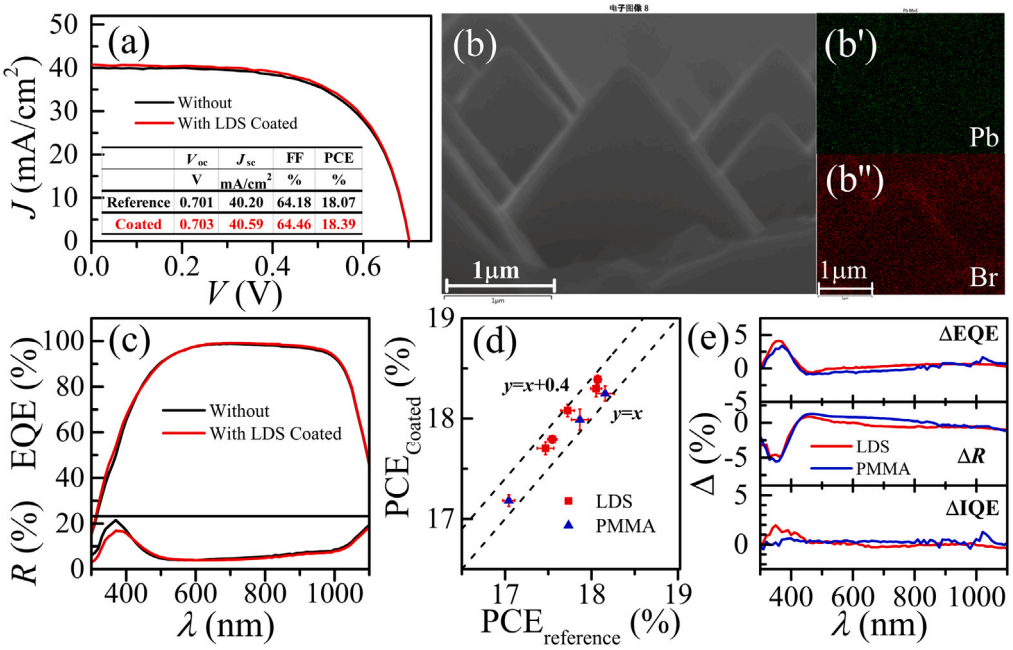

	V_{oc} V	J_{sc} mA/cm²	FF %	PCE %
Reference	0.701	40.20	64.18	18.07
Coated	0.703	40.59	64.46	18.39

Fig. 3. (a) *J-V* Curve, (b) Cross-sectional SEM and EDS mapping images, presenting the interface distribution of (b′)lead (Pb, green) and (b″)Bromine (Br, red), (c) EQE and reflectance spectra of commercial SHJ cell before (black) and after (red) coated LDS on the surface. The inset of Fig. 2(a) is their corresponding V_{oc}, J_{sc}, FF, and PCE. (d) PCE of series of SHJ before and after coated with LDS (red squares) and PMMA (blue triangles) (e) variation of EQE (*Δ*EQE, top), *R* (*ΔR*, middle), and IQE (*Δ*IQE, bottom) after coated with PMMA (blue line) and LDS (red line) layers.

of 300~410 nm. According to theoretical simulation, the decrease of *R* is from the contribution of PMMA matrix, whose refractive index (n_{PMMA} = 1.48 ~ 1.55) lies between that of air (n_{air} ≈ 1) and ITO (n_{ITO} = 1.8 ~ 2.1) [49]. Control experiments with only PMMA (without $MAPbBr_3$ NPLs) coated on the surface of SHJ solar cell shown in Fig. S14 exhibit similar variation trends of *R* to those in Fig. 3(c). Fig. S14 clearly demonstrates the overall reduction of *R* with the increasing PMMA concentration, further supporting the theoretical important role of PMMA matrix in anti-reflection. Notably, the enhancement of reflectance in the longwave region (500~800 nm in Fig. S15) is possibly from the enlargement of top angle of pyramid structure [20]. To further investigate the effect of energy down-shift of LDS layers, we also carried out the control experiments with pure PMMA covered on SHJ solar cells. Fig. 3(d) and Table S1 show the PCE of series of SHJ cells before and after covered with pure PMMA (blue triangle) and $MAPbBr_3$/PMMA-20 layer (red square). They demonstrated that the coating of pure PMMA layer leads to a PCE gain of ~0.1% absolute, but the application of $MAPbBr_3$/PMMA-20 dispersions realize a higher PCE gain, with a highest value reaching 0.36%, from initial 17.72% to 18.08%. The higher gain brought by LDS layer implies the existence of energy down-shifting role in the SHJ with LDS coating layer. Fig. 3(e) and Fig. S16 give the variation of EQE, *R*, and IQE spectra of SHJ solar cell after coated with pure PMMA (blue) and $MAPbBr_3$/PMMA-20 (red) thin film respectively. *Δ* in this figure means the spectra difference of SHJ solar cell between after and before film coated, and IQE is calculated from

$$IQE(\lambda) = \frac{EQE(\lambda)}{1 - R(\lambda) - T(\lambda)} \quad (4)$$

where $R(\lambda)$ is the reflectance and $T(\lambda)$ is transmittance (assumed to be zero due to the highly reflective back contact). Obviously, as shown in the top and middle in Fig. 3(e), in the range of 450~1100 nm, *Δ*EQE and *ΔR* give similar gain tendency for both pure PMMA and LDS coated samples, illustrating the variation of reflectance is mainly caused by PMMA matrix. Notably, although PMMA has a better AR role in the range of 300~450 nm, the addition of $MAPbBr_3$/PMMA-20 LDS layer still brings a higher gain of EQE, which is probably from the contribution of LDS effect. Hence, we also compare the variation of IQE spectra in bottom of Fig. 3(e), since it excludes the influence of reflection and depends on competitive result between parasitic absorption losses and down-shifting effects [50,51]. Clearly, *Δ*IQE of pure PMMA covered SHJ solar cell is almost equal to zero, but *Δ*IQE of LDS layer covered samples shows a maximum increase of 2% in the 300~450 nm range. However, as shown in Fig. S17, more thicker hybrid films on SHJ cell, e.g. spin coating LDS layer for 2 times, causes the decrease of PCE, which is possibly from the increase of reabsorption loss and reflectance loss caused by the thicker NPLs thin film.

Using $MAPbBr_3$/PMMA-20 as LDS layer on SHJ has successfully improved its performance, so that we further fabricate $MAPbBr_3$/PMMA-20 LDS layer on PERC solar cell (~2 cm × 2 cm, with Si_3N_4 layer) to study the applicability of LDS layers on different types of solar cells. Fig. 4(a) displays *J* – *V* curves and the PV parameters (inset of the figure) of commercial PERC before (black) and after (red) coated with $MAPbBr_3$/PMMA-20 LDS layer. The coating of LDS layer also leads to the improvement of the current density. J_{sc} increases from 38.79 mA/cm² (before) to 39.87 mA/cm² (after), leading to an improvement of 0.55% in PCE. As shown in Fig. S18, similar to results of SHJ cell, more thicker hybrid films on PERC, e.g. spin coating LDS layer for 2 and 3 times, causes the decrease of PCE. SEM and EDS elemental mapping images in Fig. 4(b)–(b″) and in Fig. S19 display that the uniformly distributed $MAPbBr_3$ NPLs are tightly attached to the surface. As shown in Fig. 4(c), the introduction of LDS layer results in the improvement of EQE and AR of PERC in the band region of 300~380 nm and 650~1100 nm, but weakening in the rest region (380~650 nm). Control experiment with only $MAPbBr_3$ NPLs (without PMMA) coated on the PERC surface in Fig. S20 displays the almost unchanged *R* but decreased EQE at short wavelengths, illustrating the antireflective and protective role of PMMA matrix for $MAPbBr_3$ NPLs from deterioration in air atmosphere. Coating pure PMMA on PERC also results in the decrease of reflectance, as shown in Figs. S21~S22. However, as observed in Fig. 4(d), the coating of pure PMMA layer (blue triangle) leads to a PCE gain of only ~0.2%, while the application of $MAPbBr_3$/PMMA-20 layer (red square) realizes a higher PCE gain, with a highest value reaching 0.7%, from initial 17.15% to 17.85%. It is worthy noting that compared to SHJ cells (see Fig. 3(e)), the coating of

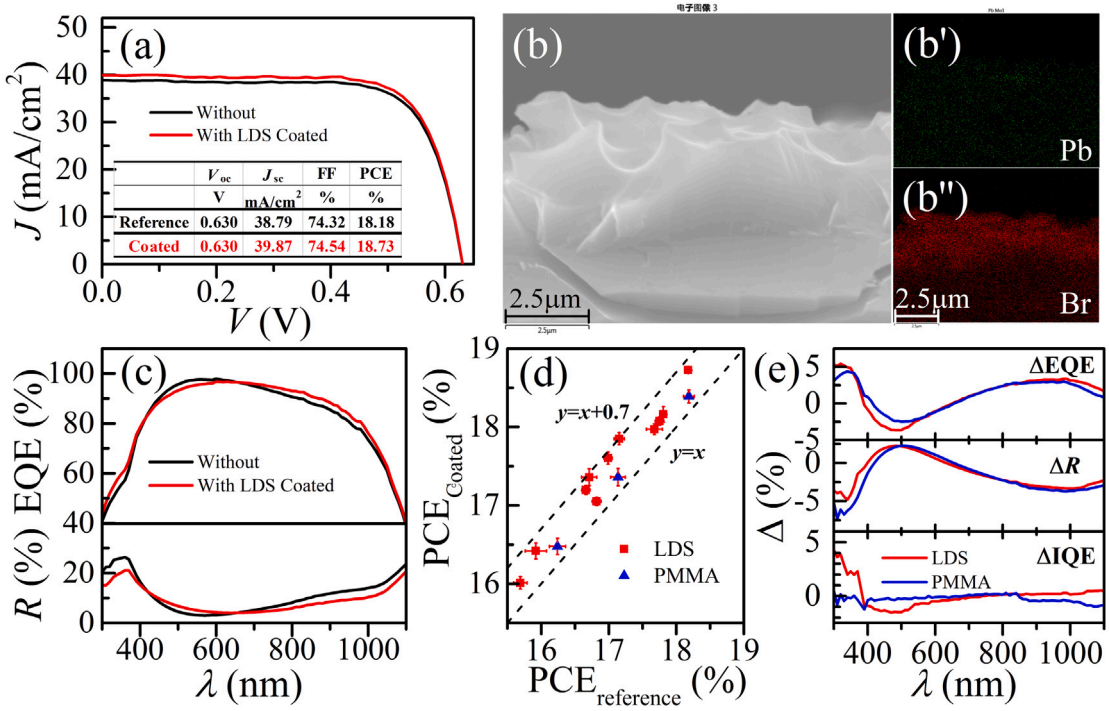

	V_{oc} V	J_{sc} mA/cm^2	FF %	PCE %
Reference	0.630	38.79	74.32	18.18
Coated	0.630	39.87	74.54	18.73

Fig. 4. (a) *J-V* Curve, (b) Cross-sectional SEM and EDS mapping images, presenting the interface distribution of (b′)lead (Pb, green) and (b″)Bromine (Br, red) and (c) EQE and reflectance spectra of commercial PERC cell before and after coated LDS on the surface. The inset of Fig. 2(a) is their corresponding V_{oc}, J_{sc}, FF and PCE. (d) PCE of series of PERC before and after coated with LDS (red squares) and PMMA (blue triangles) (e) variation of EQE (*Δ*EQE, top), *R* (*ΔR*, middle), and IQE (*Δ*IQE, bottom) after coated with PMMA (blue) and LDS (red) layers.

pure PMMA (Fig. S23) and/or $MAPbBr_3$/PMMA-20 LDS layer on PERC gives rise to the obvious improvement of EQE (Fig. 4(e), top) and AR (Fig. 4(e), middle). This difference is possibly from two facts. One is that SHJ cell possesses better AR performance than PERC, which makes it harder to obtain a higher gain of AR effect. The other is that EQE of SHJ cell (see Fig. 3(c)) at 530 nm is 93.6%, less than that (97.2%) of PERC (see Fig. 4(c)), leading to a weaker LDS effect. This variation also results in that *Δ*IQE of LDS covered samples shows a maximum 4% increase in the 300~400 nm range, much more than that of SHJ, but a slight decrease in 400~500 nm (~1% at 500 nm). The abnormal reduction in 400~500 nm is possibly induced by the relative lower PLQY (~80%) of $MAPbBr_3$/PMMA-20 NPLs (Fig. S24) in that range, which need to be further improved for enhancing the down-shifting effect.

5. Conclusion

In this work, we report an absolute PCE enhancement of about 0.3% on SHJ solar cell and 0.7% on PERC by using $MAPbBr_3$/PMMA hybrid film as a LDS layer. The used $MAPbBr_3$/PMMA NPLs solutions for LDS layer have a PLQY of over 85% (excited by 350 nm) in air atmosphere for more than 30 days, laying a foundation for the realization of effective LDS effect. According to the theoretical simulation and experimental studies, it is clear that PMMA plays the key role in the protection of $MAPbBr_3$ NPLs from degradation and in the AR of solar cell. Control experiments further demonstrate the separated contribution of LDS and AR effect provided by $MAPbBr_3$/PMMA hybrid film. Thanks to this combined effect, the application of LDS layer on mainstream Si commercial solar cell produces an obvious improvement of PCE.

CRediT authorship contribution statement

Jiayao Xu: Writing – original draft, Visualization, Validation, Methodology, Investigation, Formal analysis, Data curation. **Wei Pan:** Writing – review & editing, Visualization, Validation, Supervision, Project administration, Methodology, Investigation, Formal analysis, Conceptualization. **Wenzhong Shen:** Writing – review & editing, Supervision, Resources, Project administration, Funding acquisition, Conceptualization.

Declaration of competing interest

The authors declare that they have no known competing financial interests or personal relationships that could have appeared to influence the work reported in this paper.

Data availability

Data will be made available on request.

Acknowledgments

This work was supported by the Major State Basic Research Development Program of China (2022YFB4200101), the National Natural Science Foundation of China (11834011, 11974242), and Inner Mongolia Science and Technology Project (2022JBGS0036).

Appendix A. Supplementary data

Supplementary material related to this article can be found online at https://doi.org/10.1016/j.solmat.2023.112478.

References

[1] N.L. Panwar, S.C. Kaushik, Surendra Kothari, Role of renewable energy sources in environmental protection: A review, Renew. Sustain. Energy Rev. 15 (2011) 1513–1524.
[2] N. Kannan, D. Vakeesan, Solar energy for future world: -A review, Renew. Sustain. Energy Rev. 62 (2016) 1092–1105.

[3] E. Klampaftis, D. Ross, K.R. McIntosh, B.S. Richards, Enhancing the performance of solar cells via luminescent down-shifting of the incident spectrum: a review, Sol. Energy Mater. Sol. Cells 93 (2009) 1182–1194.

[4] M.B. de la Moraa, O. Amelines-Sarriab, B.M. Monroyd, C.D. Hernández-Péreze, J.E. Lugo, Materials for downconversion in solar cells: Perspectives and challenges, Sol. Energy Mater. Sol. Cells 165 (2017) 59–71.

[5] J. Day, S. Senthilarasu, T.K. Mallick, Improving spectral modification for applications in solar cells: A review, Renew. Energy 132 (2019) 186–205.

[6] H.J. Hovel, R.T. Hodgson, J.M. Woodall, The effect of fluorescent wavelength shifting on solar cell spectral response, Solar Energy Mater. 2 (1979) 19–29.

[7] Z. Hosseinia, N. Taghaviniab, E.W. Diau, Application of a dual functional luminescent layer to enhance the light harvesting efficiency of dye sensitized solar cell, Mater. Lett. 188 (2017) 92–94.

[8] H. Jeong, Y. Kim, S. Lee, J. Yun, J. Jang, Enhanced spectral response of CIGS solar cells with anti-reflective subwavelength structures and quantum dots, Sol. Energy Mater. Sol. Cells 194 (2019) 177–183.

[9] Y. Kim, H. Jeong, S. Kim, Y.H. Song, B.Y. Kim, J.P. Kim, B.K. Kang, J. Yun, J. Jang, Luminescent down-shifting $CsPbBr_3$ perovskite nanocrystals for flexible $Cu(In, Ga)Se_2$ solar cells, Nanoscale 12 (2020) 558.

[10] F. Sui, M. Pan, Z. Wang, M. Chen, W. Li, Y. Shao, W. Li, C. Yang, Quantum yield enhancement of Mn-doped $CsPbCl_3$ perovskite nanocrystals as luminescent down-shifting layer for CIGS solar cells, Sol. Energy 206 (2020) 473–478.

[11] B.G. Jeong, D. Hahm, J.W. Park, J.Y. Kim, H. Song, M.G. Kang, S. Jeong, G. Kang, W.K. Bae, H. Song, Colorful opaque photovoltaic modules with down-converting $InP/ZnSe_xS_{1-x}$ quantum dot layers, Nano Energy 77 (2020) 105169.

[12] E. Regalado-Pérez, N.R. Mathews, X. Mathew, Eu(III) complex-polymer composite luminescence down-shifting layers for reducing the blue-losses in thin film solar cells, Sol. Energy 199 (2020) 82–91.

[13] N.S. Satpute, C.M. Mehare, A. Tiwari, H.C. Swart, S.J. Dhoble, Synthesis and luminescence characterization of downconversion and downshifting phosphor for efficiency enhancement of solar cells: Perspectives and challenges, ACS Appl. Electron. Mater. 4 (2022) 3354–3391.

[14] M. Rwaimi, C.G. Bailey, P.J. Shaw, T.M. Mercier, C. Krishnan, T. Rahman, P.G. Lagoudakis, R. Horng, S.A. Boden, M.D.B. Charlton, $FAPbBr_3$ perovskite quantum dots as a multifunctional luminescent-downshifting passivation layer for GaAs solar cells, Sol. Energy Mater. Sol. Cells 234 (2022) 111406.

[15] C.P. Thomas, A.B. Wedding, S.O. Martin, Theoretical enhancement of solar cell efficiency by the application of an ideal 'down-shifting' thin film, Sol. Energy Mater. Sol. Cells 98 (2012) 455–464.

[16] R. Rothemunda, S. Kreuzera, T. Umunduma, G. Meinhardtb, T. Fromherza, W. Jantsch, External quantum efficiency analysis of Si solar cells with II-VI nanocrystal luminescent down-shifting layers, Energy Procedia 10 (2011) 83–87.

[17] R. Rothemund, Optical modelling of the external quantum efficiency of solar cells with luminescent down-shifting layers, Sol. Energy Mater. Sol. Cells 120 (2014) 616–621.

[18] W. Feng, J. Liu, X. Yu, Efficiency enhancement of mono-Si solar cell with CdO nanotip antireflection and down-conversion layer, RSC Adv. 4 (2014) 51683–51687.

[19] A.M. Gabr, A.W. Walker, M.M. Wilkins, R. Kleiman, K. Hinzer, Procedure to decouple reflectance and downshifting effects in luminescent down-shifting enhanced photovoltaics, Opt. Express 25 (2017) A530–538.

[20] J. Wang, F. Zhong, H. Liu, L. Zhao, W. Wang, X. Xu, Y. Zhang, H. Yan, Influence of the textured pyramid size on the performance of silicon heterojunction solar cell, Sol. Energy 221 (2021) 114–119.

[21] T. Rahman, R.S. Bonill, A. Nawabjan, P.R. Wilshaw, S.A. Boden, Passivation of all-angle black surfaces for silicon solar cells, Sol. Energy Mater. Sol. Cells 160 (2017) 444–453.

[22] M. Huang, C. Yang, Y. Chiou, R. Lee, Fabrication of nanoporous antireflection surfaces on silicon, Sol. Energy Mater. Sol. Cells 92 (11) (2008) 1352–1357.

[23] D. Zhou, D. Liu, G. Pan, X. Chen, D. Li, W. Xu, X. Bai, H. Song, Cerium and ytterbium codoped halide perovskite quantum dots: A novel and efficient downconverter for improving the performance of silicon solar cells, Adv. Mater. 29 (2017) 1704149.

[24] C. Jiang, G. Zhang, Z. Hong, J. Chen, Y. Li, X. Yuan, Y. Lin, C. Yu, T. Wang, T. Song, Y. Wang, B. Sun, Colored silicon heterojunction solar cells exceeding 23.5 % efficiency enabled by luminescent down-shift quantum dots, Adv. Mater. 35 (6) (2022) 2208042.

[25] D. Alonso-Álvarez, D. Ross, E. Klampaftis, K.R. McIntosh, S. Jia, P. Storiz, T. Stolz, B.S. Richards, Luminescent down-shifting experiment and modelling with multiple photovoltaic technologies, Prog. Photovolt., Res. Appl. 23 (2015) 479–497.

[26] J.D. Roo, M. Ibáñez, P. Geiregat, G. Nedelcu, W. Walravens, J. Maes, J.C. Martins, I.V. Driessche, M.V. Kovalenko, Z. Hens, Highly dynamic ligand binding and light absorption coefficient of cesium lead bromide perovskite nanocrystals, ACS Nano 10 (2) (2016) 2071–2081.

[27] I. Levchuk, P. Herre, M. Brandl, A. Osvet, R. Hock, W. Peukert, P. Schweizer, E. Spiecker, M. Batentschuk, C.J. Brabec, Ligand-assisted thickness tailoring of highly luminescent colloidal $CH_33NH_3PbX_3$ (X = Br and I) perovskite nanoplatelets, Chem. Commun. 53 (2017) 244–247.

[28] L. Ievgen, A. Osvet, X. Tang, M. Brandl, J.D. Perea, F. Hoegl, G.J. Matt, R. Hock, M. Batentschuk, C.J. Brabec, Brightly luminescent and color-tunable formamidinium lead halide perovskite $FAPbX_3$ (X = Cl, Br, I) colloidal nanocrystals, Nano Lett. 17 (5) (2017) 2765–2770.

[29] Q. Fu, X. Tang, B. Huang, T. Hu, L. Tan, L. Chen, Y. Chen, Recent progress on the long-term stability of perovskite solar cells, Adv. Sci. 5 (2018) 1700387.

[30] G. Niu, X. Guo, L. Wang, Review of recent progress in chemical stability of perovskite solar cells, J. Mater. Chem. A 3 (2015) 8970–8980.

[31] S. Mirershadi, S. Ahmadi-Kandjani, Efficient thin luminescent solar concentrator based on organometal halide perovskite, Dye. Pigment. 120 (2015) 15–21.

[32] A.Z. Kainarbay, T.N. Nurakhmetov, D.K. Daurenbekov, A.A. Eliseev, T.Y. Sachkova, Z.M. Salikhodzha, A.M. Zhunusbekov, Luminescent down shifting CdTe colloidal quantum dots for enhancing polycrystalline silicon solar cells, Optik 169 (2018) 41–47.

[33] Y. Li, H. Lin, J. Zeng, J. Chen, H. Chen, Enhance short-wavelength response of CIGS solar cell by CdSe quantum disks as luminescent down-shifting material, Sol. Energy 193 (2019) 303–308.

[34] Y.M. Huang, C.P. Huang, S.K. Huang, T.Y. Lee, Y.H. Liu, T.M. Chen, H.C. Kuo, C.C. Lin, The reliability and prolonged time in single-junction GaAs solar cell with perovskite quantum dots, in: Proceedings of the 47th IEEE Photovoltaic Specialists Conference, PVSC, Canada, 2020.

[35] L. Meng, L. Shi, Y. Ge, J. Tang, Y. Chen, H. Zhong, Photon management of combining nanostructural antireflection and perovskite down-shifting compositefilms for improving the efficiency of silicon solar cells, Sol. Energy Mater. Sol. Cells 220 (2021) 110856.

[36] Y. Nakamura, Y. Iso, T. Isobe, Bandgap-tuned $CuInS_2/ZnS$ core/shell quantum dots for a luminescent downshifting layer in a crystalline silicon solar module, ACS Appl. Nano Mater. 3 (2020) 3417–3426.

[37] Q. Zhou, Z. Bai, W. Lu, Y. Wang, B. Zou, H. Zhong, In situ fabrication of halide perovskite nanocrystal-embedded polymer composite films with enhanced photoluminescence for display backlights, Adv. Mater. 28 (2016) 9163–9168.

[38] S. Chang, Z. Bai, H. Zhong, In situ fabricated perovskite nanocrystals: a revolution in optical materials, Adv. Opt. Mater. 6 (2018) 1800380.

[39] L. Xia, J. Chen, K. Liao, L. Huang, Q. Li, X. Luo, Influence of laser cutting conditions on electrical characteristics of half-size bifacial silicon solar cells, Mater. Sci. Semicond. Process. 105 (2020) 104747.

[40] X. Wang, S. Wang, W. Pan, W. Shen, Efficient ultrafast energy-down-shift upon ultraviolet excitation in methylammonium lead bromide nanoplatelets, Chem. Phys. Lett. 763 (2021) 138192.

[41] L. Meng, X. Wu, S. Ma, L. Shi, M. Zhang, L. Wang, Y. Chen, Q. Chen, H. Zhong, Improving the efficiency of silicon solar cells using in situ fabricated perovskite quantum dots as luminescence downshifting materials, Nanophotonics 9 (1) (2020) 93–100.

[42] Y. Wei, X. Deng, Z. Xie, X. Cai, S. Liang, P. Ma, Z. Hou, Z. Cheng, J. Lin, Enhancing the stability of perovskite quantum dots by encapsulation in crosslinked polystyrene beads via a swelling-shrinking strategy toward superior water resistance, Adv. Funct. Mater. 27 (2017) 1703535.

[43] A. Pan, M. Jurow, F. Qiu, J. Yang, B. Ren, J. Urban, L. He, Y. Liu, Nanorod suprastructures from a ternary graphene oxide-polymer-$CsPbX_3$ perovskite nanocrystal composite that display high environmental stability, Nano Lett. 17 (2017) 6759–6765.

[44] Y. Kim, C. Wolf, Y. Kim, H. Cho, W. Kwon, S. Do, A. Sadhanala, C.G. Park, S. Rhee, S.H. Im, R.H. Friend, T. Lee, Highly efficient light-emitting diodes of colloidal metal-halide perovskite nanocrystals beyond quantum size, ACS Nano 11 (2017) 6586–6593.

[45] J. Zhu, Z. Xie, X. Sun, S. Zhang, G. Pan, Y. Zhu, B. Dong, X. Bai, H. Zhang, H. Song, Highly efficient and stable inorganic perovskite quantum dots by embedding into a polymer matrix, ChemNanoMat 5 (2019) 346–351.

[46] https://www2.pvlighthouse.com.au/calculators/OPAL%202/OPAL%202.aspx.

[47] A. Ishteev, K. Konstantinova, G. Ermolaev, D. Kiselev, D. Muratov, M. Voronova, T. Ilina, P. Lagov, O. Uvarov, Y. Pavlov, M. Letovaltseva, A. Arsenin, V. Volkov, S. Didenko, D. Saranin, A. Di Carlo, Investigation of structural and optical properties of $MAPbBr_3$ monocrystals under fast electron irradiation, J. Mater. Chem. C 10 (2022) 5821–5828.

[48] S. Wang, B.D. Weil, Y. Li, K.X. Wang, E. Garnett, S. Fan, Y. Cui, Large-area free-standing ultrathin single-crystal silicon as processable materials, Nano Lett. 13 (2013) 4393–4398.

[49] T.A.F. König, P.A. Ledin, J. Kerszulis, M.A. Mahmoud, M.A. El-Sayed, J.R. Reynolds, V.V. Tsukruk, Electrically tunable plasmonic behavior of nanocube-polymer nanomaterials induced by a redox-active electrochromic polymer, ACS Nano 8 (6) (2014) 6182–6192.

[50] L. Dworak, S. Roth, M.P. Scheffer, A.S. Frangakis, J. Wachtveitl, A thin CdSe shell boosts the electron transfer from CdTe quantum dots to methylene blue, Nanoscale 10 (4) (2018) 2162–2169.

[51] D. Du, Z. Xu, L. Wang, Y. Guo, S. Liu, T. Yu, C. Wang, F. Wang, H. Wang, The broadband and omnidirectional antireflective performance of perovskite solar cells with curved nanostructures, Sol. Energy 224 (2021) 10–17.